On the choice of boundary conditions for micromechanical simulations based on 3D imaging

Modesar Shakoor, Ante Buljac, Jan Neggers, François Hild, Thilo F. Morgeneyer, Lukas Helfen, Marc Bernacki, Pierre-Olivier Bouchard

On the choice of boundary conditions for micromechanical simulations based on 3D imaging

Modesar Shakoor[a,*], Ante Buljac[b,c], Jan Neggers[b], François Hild[b], Thilo F. Morgeneyer[c], Lukas Helfen[d,e], Marc Bernacki[a], Pierre-Olivier Bouchard[a]

[a] *MINES ParisTech, PSL Research University, CEMEF-Centre de mise en forme des matériaux, CNRS UMR 7635, CS 10207 rue Claude Daunesse, 06904 Sophia Antipolis Cedex, France*
[b] *Laboratoire de Mécanique et Technologie (LMT), ENS Cachan/CNRS/Université Paris-Saclay, 61 avenue du Président Wilson, 94235 Cachan, France*
[c] *MINES ParisTech, PSL Research University, Centre des Matériaux, CNRS UMR 7633, BP 87, 91003 Evry, France*
[d] *ANKA/Institute for Photon Science and Synchrotron Radiation, Karlsruhe Institute of Technology (KIT), D-76131 Karlsruhe, Germany*
[e] *European Synchrotron Radiation Facility (ESRF), F-38043 Grenoble, France*

Abstract

The present paper addresses the challenge of conducting Finite Element (FE) micromechanical simulations based on 3D X-ray data, and quantifying errors between simulations and experiments. This is of great interest, for example, in the study of ductile fracture as local comparisons and error indicators would help understanding the limitations of current plasticity and damage models. Standard methods used in the literature to conduct FE simulations at the microscale are often based on multiscale schemes. Relevant mechanical fields computed in an FE simulation at the specimen scale are used as boundary conditions for the micromechanical simulation, where the real microstructure is meshed from 3D X-ray images. These methods hence rely on an identification of material behavior at the macroscale, say, using force measurements and 2D surface images. In an earlier work by the authors, a method for conducting micromechanical simulations using measured boundary conditions thanks to Digital Volume Correlation (DVC) was proposed. The interest of this DVC-FE approach is that it uses solely 3D X-ray images acquired *in-situ* during the experiments. Thus,

* Corresponding author.
Email address: modesar.shakoor@mines-paristech.fr (Modesar Shakoor)

FE simulations are directly conducted at the microscale, with no dependence on specimen scale simulations or multiscale schemes. This method also includes a methodology to perform local error measurements with respect to experimental observations. In this paper, both multiscale schemes and this DVC-FE approach are applied to new experimental results on a nodular cast iron specimen with machined holes. Ductile fracture due to the nucleation, growth and coalescence of microscopic voids between the machined holes is observed *in-situ* thanks to synchrotron 3D imaging. The objective of this paper is to assess the accuracy of boundary conditions for each approach and conclude on the optimal choice. Based on both average and local error measurements, it is shown that void growth is underestimated with multiscale schemes, while predictions are significantly improved with the DVC-FE approach.

Keywords: Digital Volume correlation; Ductile fracture; Level set; Multiscale analysis; Micromechanical modeling; Microstructure meshing; X-ray laminography

---

1. Introduction

In the aim for understanding the physical nature of any phenomenon, comparison between experiments and theoretical models is used extensively [1]. In the case of ductile fracture, difficulties arise due to the competition between localization and softening events occurring at different scales [2, 3]. In particular, investigations of ductile fracture mechanisms, namely, void nucleation, growth and coalescence at the microscale require 3D observations at this scale. On the numerical side, being able to simulate these mechanisms with comparable geometric and loading conditions is still an open research topic, which is once again due to the scale at which the geometry and the loading have to be identified.

Although 3D *in-situ* experimental observations (*e.g.,* X-ray tomography and laminography) have provided valuable information for ductile fracture modeling [4, 5, 6, 7, 8, 9], numerous questions regarding comparisons between models and experiments are still to be answered. For instance, the well-known work

of Gurson [10] has motivated researchers to rely extensively on homogenization theory to model ductile fracture based on analytical [10, 11, 12, 13] or numerical procedures [14, 12, 13, 15, 16]. Even though interesting results can be obtained on average values, the applicability of these homogenized models to real 3D microstructures is quite limited due to the assumptions of idealistic microstructures and boundary conditions on which they are based [17, 18, 6, 9].

Numerical procedures at the microscale could be applied given that 3D X-ray images of the microstructure are acquired *in-situ*, that a microstructure meshing technique is available, and that boundary conditions are applied. This is a critical piece of information that will be analyzed herein. There are different ways of performing such microscale simulations:

- The most straightforward approach is Direct Numerical Simulation (DNS), where the microstructure of the whole specimen has to be meshed, hence taking into account only microscale constitutive models. Since the whole specimen is simulated, boundary conditions are applied directly at pins, as in the experiment. However, depending on specimen size, DNS can have a huge cost regarding both experiments and simulations. Scanning the whole specimen could require multiple scans at each loading step, and this large set of 3D data would then have to be meshed.

- To avoid this huge computational cost, full specimen Finite Element (FE) simulations only partially taking into account the microstructure have been considered [19, 20, 21, 22, 23, 24]. Microscale constitutive models are used in the ROI where the microstructure is meshed, while macroscopic homogeneity is assumed in the remainder of the specimen. Thus, an appropriate macroscale constitutive model has to be defined and identified for this out-of-ROI homogeneous material. This approach will be referred to as strong FE (sFE) coupling.

- Opposed to the previous approach in which the ROI mesh is directly embedded within the specimen mesh, the two FE calculations can be weakly coupled. In this weak FE (wFE) approach [25, 26, 27], the specimen scale

simulation assumes a homogeneous material in the whole domain. A relevant mechanical field is then transferred from this first simulation to the second simulation at the ROI scale, where the microstructure is meshed. This mechanical field defines the boundary conditions for the micromechanical simulation. These conditions can use displacements, forces, or a combination of both.

- In a recent work [28], an alternative option for performing microscale simulations was proposed. Digital Volume Correlation (DVC) was used in order to measure displacement fields between 3D X-ray images taken at consecutive loading steps [29, 30, 31]. The DVC technique is based on tracking the natural image contrast, herein originating from the heterogeneous microstructure. FE simulations were conducted by applying measured DVC displacements to the boundaries of the meshed ROI. The difference between FE results and DVC displacement fields inside the FE domain could be assessed. Additionally, a better quantification of the error produced by FE models was obtained by computing gray level residuals based on FE and DVC displacement fields. An advantage of this so-called DVC-FE method is that no specimen scale simulation is required, thus no macroscale constitutive model has to be identified. Yet, it requires a thorough uncertainty assessment regarding DVC measurements.

The present paper aims at showing the interest of the DVC-FE approach and compare its predictive capability with simulations at the microscale based upon either weak or strong FE couplings. One key aspect is related to the boundary conditions that are applied to the simulated ROI where the microstructure is meshed. This investigation is conducted with *new* experimental results using nodular graphite cast iron specimens with a geometry inspired from Ref. [5]. A first test (A) was performed using small loading steps in order to obtain accurate force measurements and 2D surface images to be exploited thanks to global Digital Image Correlation (DIC). The second test (B) was performed using larger loading steps since it was conducted in a synchrotron facility. For

this second test, both 3D X-ray scans of the ROI and 2D surface images were acquired (see Figure 1).

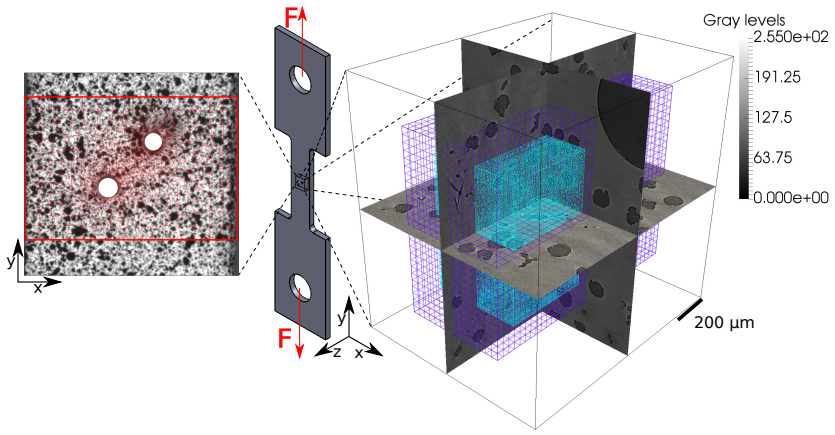

Figure 1: Schematic view of the sample with zoomed region between the holes showing on the right: DVC (blue) and FE (cyan) meshes plotted over the corresponding cast iron microstructure in isometric view. On the left: surface image with speckle pattern and DIC mesh from test (B)

While the DVC-FE methodology presented above uses directly and solely the 3D X-ray data, the two alternatives to obtain boundary conditions for ROI calculations considered in this paper (*i.e.,* wFE and sFE) rely on force measurements and 2D surface images. Force measurements are used to identify the behavior of the material at the specimen scale, as well as 2D surface images thanks to a recent Integrated-DIC framework [32]. In the wFE method, an FE simulation of the experiment at the specimen scale is conducted, and calculated displacement fields are used to drive a second FE calculation at the ROI scale. In the sFE method, the ROI is embedded and meshed directly inside the specimen mesh and only one FE simulation is conducted. In this second method, the material behavior is modeled using microscale constitutive models in the ROI, while macroscale constitutive models are used in the rest of the domain.

The aforementioned approaches with weak (wFE) and strong (sFE) couplings between specimen and ROI calculations are applied to a real 3D microstructure observed thanks to 3D *in-situ* laminography experiments. To the

best of the authors' knowledge, this is the first time such simulations are conducted and compared locally to experimental observations, this last point being possible thanks to gray level residual computation. The results are then compared to those obtained using the DVC-FE approach [28], showing the interest of this methodology. Details regarding the material, the experiments and the numerical method used for ROI calculations are presented in Section 2, while the technical implementation of each approach for boundary conditions is described in Section 3. The results are presented and compared based on error measurements with respect to experimental images in Section 4.

2. Experimental and numerical framework

2.1. Experiments

The material used in this study is a commercial nodular graphite cast iron with the serial code EN-GJS-400. It features a ferritic matrix and graphite nodules at the microscale (see Figure 2), with no significant porosity in the initial state. Under tensile loading, ductile fracture is known to be mainly driven by early debonding of the nodules from the matrix and coalescence of the subsequent nucleated voids [33, 34, 35]. Previous works [33, 36, 37, 34] suggest to model the nodules as voids, as their load carrying capacity is very low under tensile loading. This assumption is made herein meaning that at the microscale the material is considered as a two-phase microstructure with a ferritic matrix and voids.

The specimen geometry, which is inspired by the work of Weck et al. [5], is shown in Figure 2. The holes have been machined via Electrical Discharge Machining (EDM). The testing device applies the load by manually controlling the displacement via screw rotation.

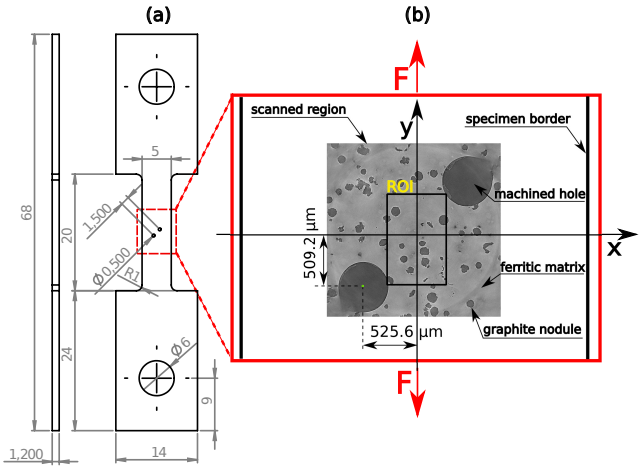

Figure 2: (a) Sample geometry with the scanned region between the pin holes; (b) section of the reconstructed volume with ROI position

Test (A) is conducted as a pre-test for test (B) to study in detail the particular sample behavior (*i.e.,* to assess the load levels for the scanning procedure). Therefore, identical sample geometry and material are used for test (B). The load/displacement curve for test (A) is shown in Figure 5(b). Load data acquired during test (A) refer to peak values. The time lapses between peak loads and laminographic scans are less than 10 minutes for test (B).

In test (B) after applying each loading step, a scan is acquired while the sample is rotated about the laminographic axis (*i.e.,* parallel to the specimen thickness direction). This axis is inclined with respect to the X-ray beam direction by an angle $\theta \approx 60°$. The 3D images used in this work were obtained at beamline ID15A of the European Synchrotron Radiation Facility (ESRF, Grenoble, France) with a 60-keV white beam, using 3,000 projections per scan. The series of radiographs acquired is then used to reconstruct 3D volumes by using a filtered-back projection algorithm [38]. The parameter optimization has been performed automatically using a GPU-accelerated implementation of this algorithm [39]. The reconstructed volume has a size of $1600 \times 1600 \times 1600$ voxels. The physical size (length) of 1 cubic voxel is equal to 1.1 μm. After scanning the undeformed state (0), 12 additional scans are acquired during the stepwise

loading procedure, where the last scan corresponds to the fully opened final crack.

The scanned region incorporates two holes while the ROI employed in DVC and FE calculations is mainly concentrated in the ligament between the holes (see Figures 1 and 2). Since the two machined holes have diameters of 500 μm, the nodule population (treated as voids in the FE calculations) in the ligament area with the characteristic size of 60 μm can be considered as a secondary void population. Hence, subsequent concurrent micro and macro plasticity and damage localization phenomena can be observed. In Ref. [5], the authors used machined holes of micrometer size, which made impossible the observation of the secondary void population (this limitation on the size of observable voids is actually due to current imaging techniques [40]). Here, the larger size of the holes, and the large size of the graphite nodules allow for such observations. This is illustrated in Figure 3 where mid-thickness sections of the reconstructed volume for the three different load stages are shown. As a consequence of the mentioned multiscale flow conditions, classical void coalescence mechanisms are accompanied by sheet coalescence between the two machined holes that is observed in the last loading step (deformed state (11)).

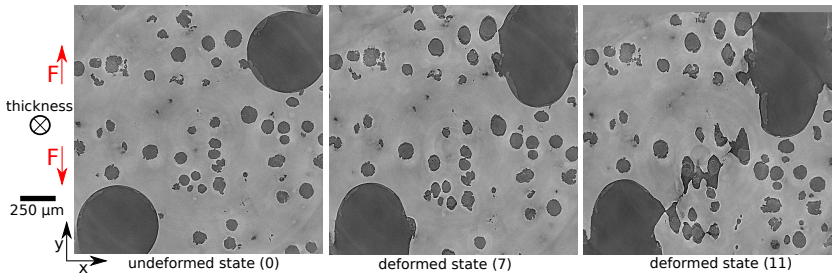

Figure 3: Mid-thickness section of the reconstructed volume for three different loading steps

2.2. FE mesh of the microstructure

The framework used for microscale FE simulations is based on previous developments presented in Refs. [41, 42, 43, 44, 45]. As explained in Ref. [28], the ROI used for FE simulations has to be included in all DVC domains through-

out each loading step. Otherwise displacement fields would not be available as boundary conditions on the whole boundary of the FE mesh. This requirement is necessary for the DVC-FE approach but also for other approaches in order to allow for comparisons with experimental observations. In practice, in order to be as representative as possible, a 3D box as large as possible is chosen. This 3D box has to be small enough to remain in all scanned regions throughout loading. The image meshing technique used to model the microstructure observed in the experimental 3D images starts with standard image processing operations [46, 47]. They consist of smoothing the data, applying a gray value threshold to separate matrix and voids, and then converting these binary data into a signed distance function. The latter is interpolated to a first mesh of uniform size (*i.e.,* 10 μm) of the FE ROI using trilinear FE interpolation (*i.e.,* the image is considered as a hexahedral grid where the voxels are nodes). The resulting signed distance function is then regularized based on a recently proposed parallel reinitialization algorithm [43], and used as an intermediary to locate the interface [45]. This mesh generation step is combined with an adaption step taking into account the local maximum curvature of the interface [44]. These different steps are summarized in Figure 4.

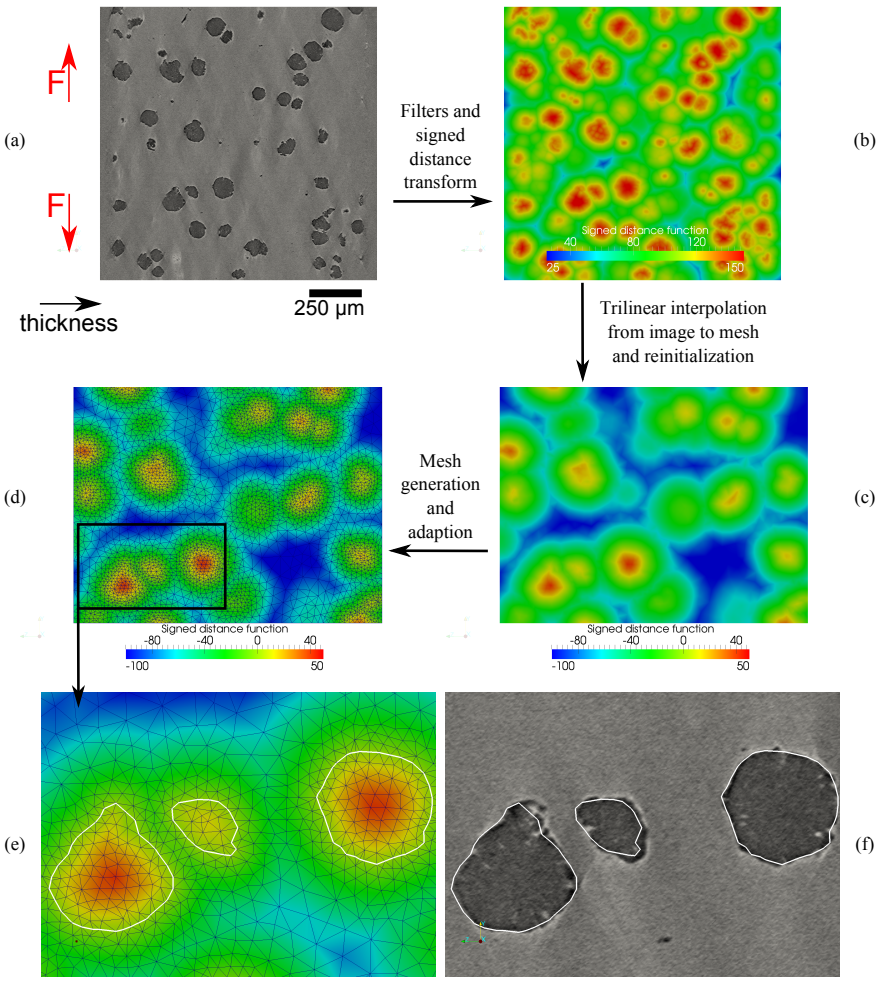

Figure 4: Image immersion and meshing. (a) Initial laminography 2D section, (b) signed distance function computed thanks to image processing, (c) signed distance function interpolated and reinitialized on the FE mesh [43], (d) conforming FE mesh generated and adapted to interfaces and local maximum curvature, (e) zoom on the FE mesh, (f) comparison between initial laminography 2D section and interfaces in the final FE mesh (in white)

Parameters of the final mesh are defined to have a size of 10 μm close to matrix/void interfaces, and 50 μm at a distance of 100 μm from any interface, the transition in this layer being linear. It can be observed qualitatively in Figure 4 that the FE approximation of the geometry is really close to experimental data. A more thorough analysis of the sensitivity of the results to meshing parameters

was assessed (not reported herein) and revealed this influence to be negligible, as already validated in a previous study for a different experiment on the same material [28].

2.3. Constitutive laws and parameters

2.3.1. Microscale model

The microscale simulations need material models for the graphite nodules and the ferritic matrix. As stated in the introduction, graphite nodules are modeled as voids [33, 36, 37, 34], while the ferritic matrix is considered as elastoplastic with power law hardening

$$\sigma_0(\bar{\varepsilon}) = \sigma_y + K\,(\bar{\varepsilon})^n \tag{1}$$

where $\bar{\varepsilon}$ is the equivalent (von Mises) plastic strain, σ_y the yield stress, K the plastic consistency and n the hardening exponent. A particularity of the present numerical method is that voids are meshed and defined as a purely elastic material with very low Young's modulus with respect to the matrix. A sensitivity analysis regarding this Young's modulus was conducted [28] showing that a ratio of $1,000$ between this modulus and that of the matrix was sufficient. The properties of the matrix are deduced from stress/strain curves [36] and presented in Table 1. These data are based on tensile experiments on a purely ferritic material. Thus, it is possible that the actual behavior of the matrix be more complex. An interesting perspective to the present work would be to use micromechanical calculations and local error measurements to study more appropriate microscale constitutive models and identify more realistic material properties.

Table 1: Elasto plastic properties of the ferritic matrix

E (GPa)	ν	σ_y (MPa)	K (MPa)	n
210	0.30	290	382	0.35

Mechanical solution of the equilibrium equations is based on a mixed velocity-pressure formulation solved using a $P1^+/P1$ element to avoid locking issues [48].

The nonlinear behavior of the matrix requires a Newton-Raphson scheme both for numerical integration of the plastic law and global equilibrium [49]. In order to handle large deformations, an updated Lagrangian scheme is used and the velocity field resulting from the mechanical solution is applied to move mesh nodes. An advanced mesh motion technique is necessary and plays a key role in micromechanical simulations. Since the latter will be driven herein by boundary conditions reproducing as accurately as possible what is observed in Figure 3, large distortions will occur inside the ROI. As a result, mesh quality will deteriorate, thus affecting the accuracy of FE solutions. Flip of elements may also occur. These issues are handled herein thanks to an automatic mesh motion and adaption method developed in previous works [43, 44, 45]. This method was designed to preserve at best the local distribution of volumes between the matrix and the voids while handling large void growth and complex topological events such as void coalescence.

2.3.2. Macroscale model

Both wFE and sFE methods require the identification of material parameters $\{\mathbf{p}\}$ based on experimental measurements acquired during test (A). In the case of wFE, these material parameters are used in the whole domain for the calculation at the specimen scale of test (B). In the case of sFE, these parameters are only used for the homogenized out-of-ROI material, while microscale material parameters (Table 1) are used inside the ROI. The identification of material parameters can be performed only using force measurements, or using both force measurements and 2D surface images. The two approaches are detailed hereafter.

Load data

A first identification is conducted using standard global optimization methods [50, 51], where the objective function is defined as [52]

$$E(\mathbf{F}(\mathbf{u})) = \frac{\sqrt{\int_{\mathbf{0}}^{\mathbf{U}} \left(\mathbf{F}(\mathbf{u}) - \mathbf{F}^{exp}(\mathbf{u})\right)^2 \mathrm{d}\mathbf{u}}}{\sqrt{\int_{\mathbf{0}}^{\mathbf{U}} \mathbf{F}^{exp}(\mathbf{u})^2 \mathrm{d}\mathbf{u}}} \tag{2}$$

where the forces obtained in an FE simulation $\mathbf{F}$ are compared with the sum of reaction forces measured during the experiment $\mathbf{F}^{exp}$, with an integral on the loading path $[\mathbf{0}, \mathbf{U}]$. Therefore, only load data acquired during test (A) are taken into account. Note that the displacement $\mathbf{u}$, and all displacements mentioned in this paper, are measured via 2D DIC [53, 54, 55]. These values were determined directly at the upper and lower parts of the mesh presented in Figure 5(a). The force/displacement curve based on measurements and simulations is shown in Figure 5(b). The experimental data were acquired up to final failure, but the last loading steps of test (B) were discarded for this inverse analysis because no micromechanical simulation is carried out up to final failure in Section 4. The force/displacement curves show that the numerical approximation is very good, but here only the macroscopic force is compared. Local measurements are considered in the sequel.

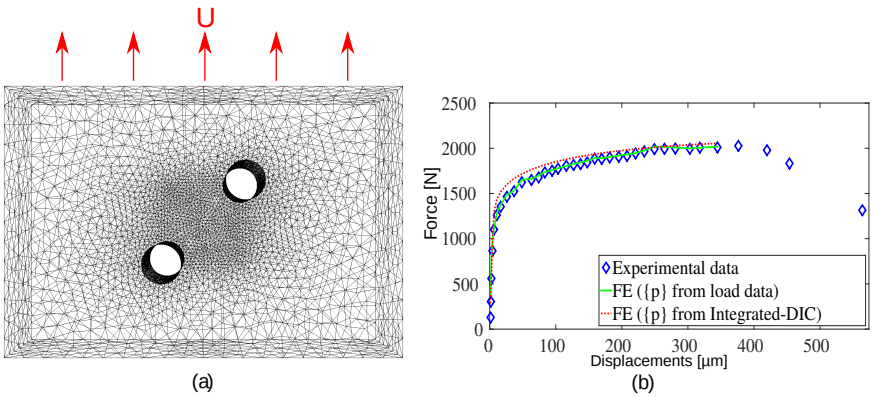

Figure 5: Identification of macroscopic material parameters based on test (A) data. (a) Mesh used for specimen scale calculations, (b) comparison between the simulated force/displacement curves and experimental data

Load data and pictures

In order to obtain more realistic material properties more advanced identification techniques can be considered. In Integrated-DIC or DVC [32, 56, 57], both pictures (*i.e.,* 2D surface images from test (A)) and load (*i.e.,* force measurements from test (A)) data are taken into account. Integrated DIC requires

displacement fields to be fully mechanically admissible, *i.e.,* satisfy equilibrium for the chosen constitutive law. Since material parameters are sought, the corresponding sensitivity fields [58] are also needed. The displacement fields are parameterized with the sought corrections $\{\delta\mathbf{p}\}$ to the current material parameters $\{\hat{\mathbf{p}}\}$ over the whole loading history t

$$\mathbf{u}(\mathbf{x}, t, \{\mathbf{p}\}) = \sum_t \sum_p u_p(\{\mathbf{p}\}, t)\boldsymbol{\Psi}_p(\mathbf{x}) \tag{3}$$

where the kinematic degrees of freedom u_p are linked to the sought material parameters via sensitivities

$$u_p(\{\mathbf{p}\}, t) = u_p(\{\hat{\mathbf{p}}\}, t) + \left\{ \frac{\delta u_p}{\delta\{\mathbf{p}\}}(\{\hat{\mathbf{p}}\}, t) \right\}^T \{\delta\mathbf{p}\}. \tag{4}$$

The kinematic sensitivities are collected in matrix $[\mathbf{S}_u(t)]$ and evaluated for each loading step t via FE simulations in which measured displacements are prescribed on the top and bottom boundaries of the considered ROI. These Dirichlet boundary conditions are measured *a priori* by conducting global DIC on 2D images from test (A). Simultaneously, the load measurements gathered in vector $\{\mathbf{F}^{exp}\}$ are compared with the resultant forces $\{\mathbf{F}^{FE}\}$ from the corresponding FE simulation. As for the kinematic part, the load sensitivity matrix $[\mathbf{S}_F(t)]$ to the sought material parameters is computed to update $\{\delta\mathbf{p}\}$ from the current estimate $\{\mathbf{F}^{FE}(\{\hat{\mathbf{p}}\})\}$ of the reaction forces. Since both images and loads are used in a single approach and due to different physical natures of the data a Bayesian framework is considered herein, in which each piece of data is weighted by its variance and covariance with all the other data [32, 57].

The Integrated-DIC code used herein is an in-house Matlab implementation with C++ kernels (*i.e.,* Correli 3.0 [59]) while the accompanying FE simulations are performed using the commercial package Abaqus/Standard. More details about mechanical correlation can be found in Ref. [32]. Due to very low sensitivity the Poisson's ratio had to be set in Integrated-DIC to its initial value of 0.28 while the other elastoplastic parameters have been identified.

Material parameters obtained using both identification procedures are given in Table 2. Though these parameters may seem to differ notably, the influence

of this difference is significant only at low (*i.e.,* < 0.2) and very large (*i.e.,* > 1) equivalent plastic strain, the latter not being experienced herein. Hence, the results are not expected to strongly depend on the choice of identification procedure apart from the first loading steps, as illustrated in Figure 5(b).

Table 2: Elastoplastic properties of nodular cast iron obtained using two inverse analyses on test (A). The first one is only based on load data. Integrated-DIC also uses kinematic data

Method	E (GPa)	ν	σ_y (MPa)	K (MPa)	n
Load data	187	0.28	64	520	0.19
Integrated-DIC	136	0.28	220	410	0.33

3. Boundary conditions

As explained in Section 1, three different techniques will be used to determine the boundary conditions of FE simulations at the microscopic scale. Two procedures, namely, wFE and DVC-FE, consist of computing or measuring displacement fields and then applying them as Dirichlet boundary conditions on the whole boundary of the FE mesh of the ROI of the microscale calculations. The third procedure (*i.e.,* sFE) has the ROI mesh embedded within the sample geometry and the whole computation is run in a single step. The three approaches and their implementation are detailed hereafter.

3.1. Weak Finite Element (wFE) technique

An application of the wFE technique to ductile fracture with meshed microstructure can be found in Ref. [27]. The objective of this study was to assess the influence of macroscopic loading conditions on the microstructure, especially regarding damage localization around inclusions. Although the real microstructure was meshed from a 3D X-ray image of the material, there was no comparison with experiments regarding micromechanical calculations, as proposed herein.

In the present work, a first macroscopic simulation of test (B) is conducted at the specimen scale. The material is considered as homogeneous and modeled

using the same elastoplastic model with the power law hardening defined in Equation (1) and the two sets of material parameters given in Table 2. Since specimens used in tests (A) and (B) had identical geometries, the same mesh as in Figure 5(a) is used. The displacement field between each consecutive loading steps where 3D X-ray scans were acquired is stored in the reference configuration. These displacements are then interpolated at the boundaries of the ROI during a second FE simulation at the microscale by means of linear interpolation (both meshes being exclusively composed of tetrahedra).

3.2. Strong Finite Element (sFE) technique

In the sFE method, a single FE simulation is carried out. The microstructure is directly meshed within the specimen mesh, with a progressive mesh coarsening from the very fine mesh close to the microstructure to the coarse mesh out of the ROI. Such mesh can be quite complex to build with conventional meshing tools, especially when a real microstructure is considered. This approach has been used for small compact tension specimens in Refs. [19, 21, 24]. The microstructure of the studied high strength steel featured two populations of particles and voids, namely, one of micrometer size and one of sub-micrometer size. In these studies, only the major population was meshed and simulated with the sFE method. Promising results were obtained by using a damage model inside the matrix material in order to account for sub-micrometer size voids. However, in the absence of local error measurements and *in-situ* experiment, it was not possible to quantify locally the accuracy of this micromechanical model.

In order to avoid the difficulties linked to real microstructures and their randomness, experiments on tensile specimens with machined micrometer size holes were proposed [5]. Simulations based on this experimental procedure were performed [60, 22]. Because the position of the holes and their size was part of the specimen geometry, generating meshes adapted to the microstructure was simplified. However, these studies revealed an influence of a minor void population, which could not be meshed.

The specimen geometry with two machined holes used in the present work

is directly inspired from Ref. [5]. Thanks to the millimeter size of the machined holes, and the micrometer resolution of synchrotron laminography, it is proposed herein to mesh both void populations, namely, the machined holes and the nodules (considered as voids herein). This is illustrated in Figure 6. This mesh is similar to that shown in Figure 5(a), with the difference that this time it incorporates the ROI with its microstructure. In the ROI, the material properties correspond to those of Table 1, while in the rest of the specimen the two sets of material properties given in Table 2 are considered. Compared to other approaches, this method adds significant computation time, as illustrated by the used mesh of ≈ 1.5 million elements in Figure 6. However, it has the advantage that ductile fracture can be studied simultaneously at two scales.

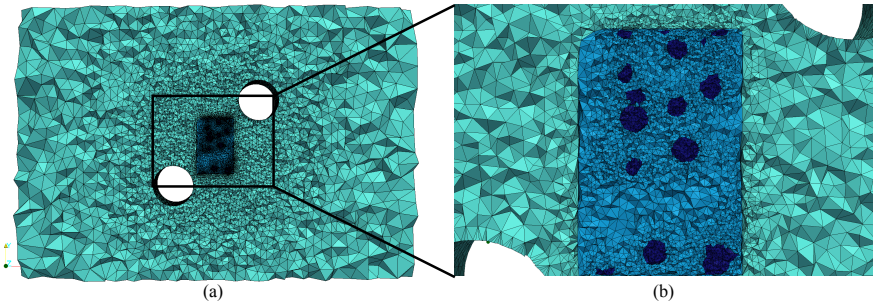

Figure 6: Inside view of the mesh used in sFE calculations. (a) Full specimen, (b) zoom on the ROI. The three shades of blue represent, from lighter to darker, the homogenized out-of-ROI material, the matrix, and the voids

3.3. Digital Volume Correlation - Finite Element (DVC-FE) technique

DVC used herein is an extension of global 2D DIC [53, 54]. The reconstructed volume is represented by a discrete gray level field of the spatial (voxel) coordinate $\mathbf{x}$. The principle of DVC lies in matching the gray levels f in the reference configuration with those of the deformed volume g such that their conservation is obtained

$$f(\mathbf{x}) = g[\mathbf{x} + \mathbf{u}(\mathbf{x})] \tag{5}$$

where $\mathbf{u}$ is the displacement field with respect to the reference volume. In real experiments the strict conservation of gray levels is not satisfied, especially in

laminography where deviations appear not just due to acquisition noise but also due to reconstruction artifacts because of missing information [61]. Consequently, the solution consists in minimizing the gray level residual $\rho(\mathbf{x}) = f(\mathbf{x}) - g[\mathbf{x} + \mathbf{u}(\mathbf{x})]$ by considering its L2-norm with respect to kinematic unknowns associated with the parameterization of the displacement field. Since a global approach is used in this work, the whole ROI is considered, the global residual Φ_c^2

$$\Phi_c^2 = \sum_{ROI} \rho^2(\mathbf{x}) \tag{6}$$

is minimized with respect to the unknown degrees of freedom u_p, the displacement field being written as

$$\mathbf{u}(\mathbf{x}) = \sum_p u_p \mathbf{\Psi}_p(\mathbf{x}) \tag{7}$$

where $\mathbf{\Psi}_p(\mathbf{x})$ are the chosen displacement fields for the parameterization of $\mathbf{u}(\mathbf{x})$. Among a whole range of available fields, finite element shape functions are particularly attractive because of the link they provide between the measurement of the displacement field and numerical models. Thus, a weak formulation based on hexahedral finite elements with trilinear shape functions is chosen [62].

Conducting DVC analyses with the full size reconstructed volumes is computationally too demanding. Therefore only a part of the reconstructed volume called DVC ROI is considered herein, as shown in Figure 2. Additionally, to be able to keep large DVC ROI sizes, the original reconstructed volumes are *a priori* coarsened, *i.e.,* each 8 neighboring voxels are averaged to form one supervoxel. By doing this, file sizes are decreased by a factor of 8.

The DVC resolution is evaluated by correlating two scans of the unloaded sample (0) with (denoted "rbm") and without (denoted "bis") a rigid body motion (RBM) applied between the acquisitions. Due to the noise contribution and reconstruction artifacts, these two volumes are not identical. Therefore, the measured displacement field accounts for the cumulated effects of laminography and DVC on the measurement uncertainty [63]. The uncertainty values are evaluated by the standard deviation of measured displacement fields. Fig-

ure 7 shows the standard resolution levels for different element sizes ℓ expressed in supervoxels. Decreasing the element size is followed by an increase of the displacement resolution [53, 1, 54, 64]. The element size used in this work is $\ell = 16$ supervoxels (length) for all three directions, which yields a standard displacement resolution of 0.25 supervoxel. This value represents the limit below which the estimated displacement levels are not trustworthy.

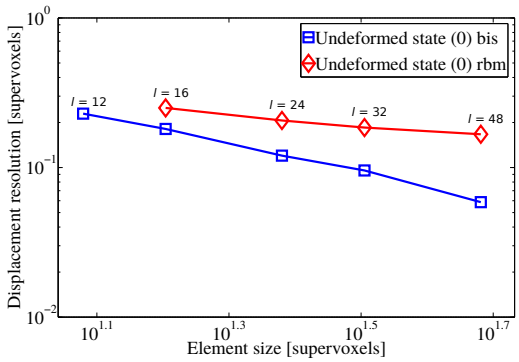

Figure 7: Standard displacement resolutions as functions of the element size ℓ expressed in supervoxels for two different scans

Successful DVC registrations have been obtained for the first 9 incremental (*i.e.,* between Step $n-1$ and Step n) loading steps and they have been used for DVC-FE boundary conditions. The DVC displacement fields are interpolated at each loading step onto the FE mesh of the ROI using trilinear interpolation (*i.e.,* identical to shape functions of DVC measurements).

4. Results

In this section, results using the DVC-FE approach are first presented and discussed, as comparisons with experiments are qualitatively and quantitatively possible. Then, comparisons with other approaches are proposed.

All micromechanical simulations (wFE, sFE, and DVC-FE) were performed on a cluster of two nodes with a 1.2 GHz Intel Xeon 20-core processor and 64 GB

RAM each. These simulations included ≈ 100 voids meshed with ≈ 1 million elements (≈ 1.5 million elements for the sFE simulation). The computation time remained close to one hour even for the sFE simulation. This quite low computation time is very promising in the perspective of applying inverse analyses at the microscale to identify micromechanical properties, especially regarding coalescence modeling. This is helped by the fact that the three approaches avoid the requirement of meshing the microstructure of the whole specimen, as in DNS. In the present case, considering the ratio between the volume of the out-of-ROI material and the volume of the ROI in Figure 6, the number of elements that a DNS calculation would require can be estimated at ≈ 100 million elements. Although such calculation is not conducted herein, the aforementioned computation time shows that it could be in the very near future, at least regarding the numerical part, thanks to the proposed methods and High Performance Computing (HPC) capabilities demonstrated in this paper. However, the wFE, sFE, and DVC-FE approaches are, by far, more efficient, as the microstructure has to be modeled only inside the ROI in the FE simulations.

4.1. DVC-FE coupling

The results using the DVC-FE approach are shown in Figure 8, where both void growth and plastic strain are observed.

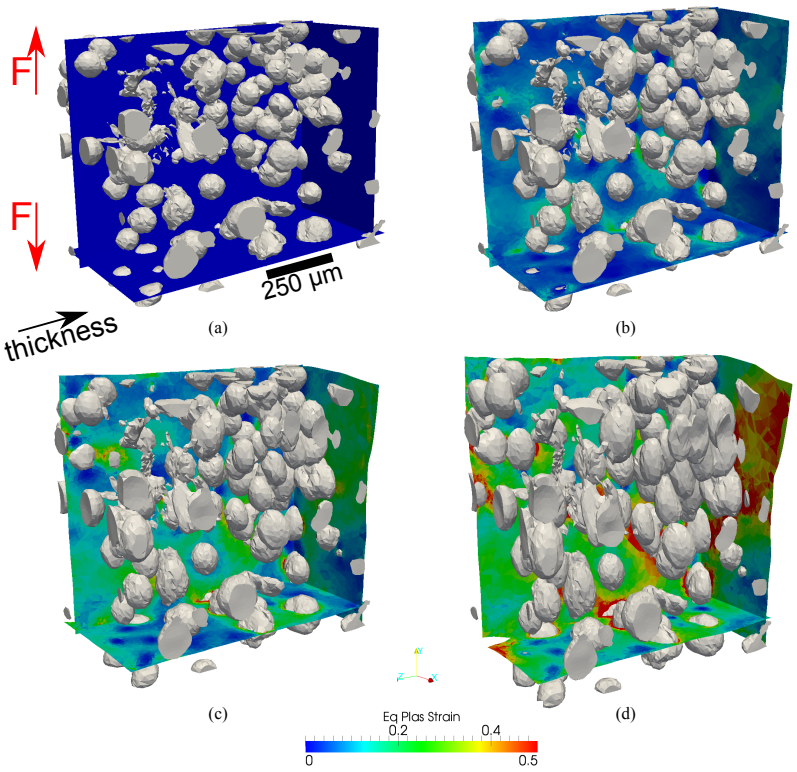

Figure 8: ROI calculation results using the DVC-FE approach showing the 3D meshed voids and the equivalent plastic strain on sections when: (a) $u = 0$ (undeformed state), (b) $u = 83$ μm, (c) $u = 192$ μm, (d) $u = 321$ μm

Errors are be assessed first qualitatively, for example by comparing the X midsection of the ROI with experimental images, as shown in Figure 9. Since DVC boundary conditions are expected to follow experimental images, the matrix/void interfaces in the simulation (in white in the figure) can be superimposed on these images and compared. This figure reveals that interfaces are overall very accurately meshed and tracked during the simulation, up to the last loading step. However, there is an irregularity in the material, namely a non spherical void in the top left region of Figure 9. In the undeformed state, this defect is already poorly captured by the meshing technique due to its very small size, and this error accumulates during loading. The same remark applies

to small voids that can be seen in the experimental image in Figure 9(a), but not in the numerical approximation. This figure shows that void growth in the simulations compares well with what is observed in X-ray images.

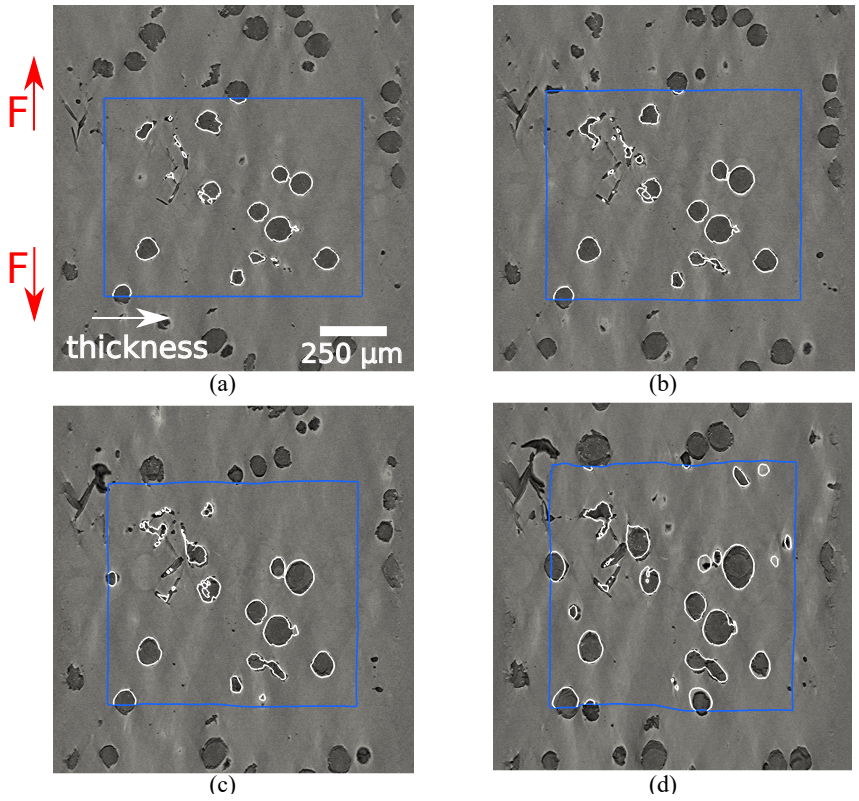

Figure 9: ROI (blue line) calculation results using the DVC-FE approach comparing the numerical matrix/void interface (white line) with experimental images for the X midsection when: (a) $u = 0$ (undeformed state), (b) $u = 83$ μm, (c) $u = 192$ μm, (d) $u = 321$ μm

For each pair of consecutive loading steps, the scan acquired for the second step can be deformed back with the displacement field obtained by the ROI calculation and the result can be compared with the scan acquired at the first step. That is, by means of a newly developed tetrahedral-DVC code [59, 57] FE solutions with corresponding tetrahedral meshes are directly imported in the reconstructed volumes frame where the displacement results are interpolated voxel-wise and the corresponding deformed volume $g(\mathbf{x})$ is corrected by the

computed displacement field $\mathbf{u}_{FE}(\mathbf{x})$. The gray level residuals, *i.e.,* differences between the reference volume $f(\mathbf{x})$ and corrected deformed volume $g(\mathbf{x}+\mathbf{u}(\mathbf{x}))$ can then be compared for DVC *and* FE computations, enabling quantitative and local error measurements. This is shown in Figure 10 as standard deviation of residual fields (normalized by dynamic range of the volume, *i.e.,* 256 gray levels) for DVC and DVC-FE calculations. These residuals remain very close to those observed in the resolution analysis for which no strains occurred. Therefore the DVC results are deemed trustworthy.

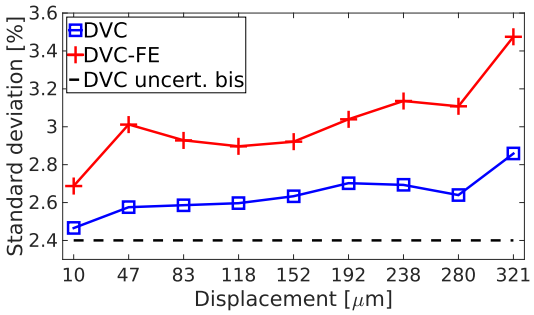

Figure 10: Standard deviation for the dimensionless gray level residual fields for all loading steps. For comparison purposes, the dashed line corresponds to the resolution analysis for the so-called "bis" case (see Subsection 3.3)

Note that the DVC-FE curve is not expected to lie below the DVC one, since the latter is used to drive the former. The error produced by micromechanical models inside the DVC-FE domain is low and it slightly increases at late loading steps (from $\approx 15\%$ initially to $\approx 20\%$ in late loading steps). A look at the Z midsection in Figure 11(a-b) reveals that these differences between simulations (DVC-FE) and experiments (DVC) are concentrated around interfaces. This is expected due to plastic localization. The growth of a minor void population and damage at a lower scale are certainly also an explanation. These minor voids cannot be observed due to the resolution of the synchrotron imaging technique used herein. In Ref. [34] they have been observed experimentally using scanning electron microscopy of fractured surfaces for a similar material. Once the minor voids are imaged with sufficient resolution, the present DVC-FE frame-

work would allow to model them. Hence, the development and application of higher resolution techniques, such as nanolaminography, would be interesting in order to check these assumptions. Yet, the present error measurements already serve as a basis for modeling and identification of more advanced plasticity and damage models, which will be considered in future work.

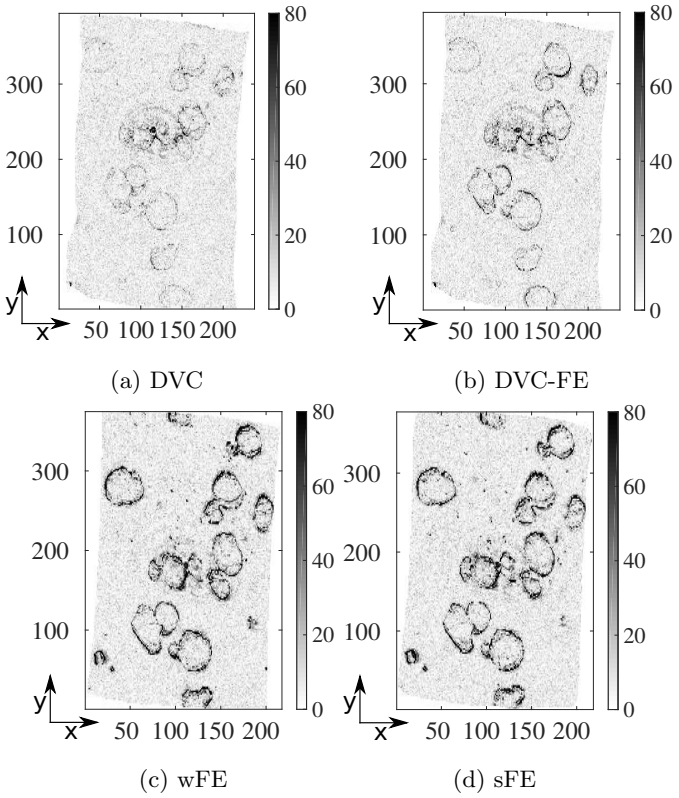

Figure 11: Absolute gray level differences at the Z midsection after correction with DVC (a), DVC-FE (b), wFE (c) and sFE (d) displacements for the ninth loading step. Note that due to different rigid body motions for each simulation, the Z midsections slightly differ

Once the absolute errors in terms of gray level residuals are estimated, relative comparisons can be shown. DVC displacement fields are applied to the boundaries of the FE domain, but they are also available inside the domain. Hence, DVC and FE kinematic fields can also be interpolated on the same mesh and directly compared as shown in Figure 12(a). Again, it is confirmed that the

main differences are concentrated in the debonding zones, while the differences close to the boundaries are mostly zero.

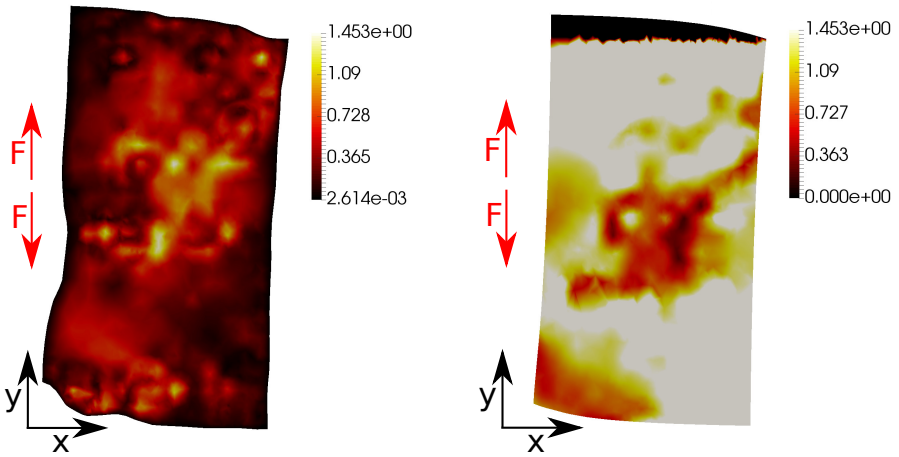

Figure 12: Mid-section normal to z-direction showing absolute difference between: (a) DVC and DVC-FE displacement fields, (b) DVC and wFE displacement fields for the ninth loading step. The black area at the top of sub-figure (b) represents a zone out of the DVC ROI. The color bar range is set according to the data set from sub-figure (a) in order to have more convenient visual comparison. The displacement difference is expressed in supervoxels (1 supervoxel $\longleftrightarrow$ 2.2 μm)

Although the results using the DVC-FE method are promising, several aspects remain to be improved. In particular, Figure 9 as qualitative and Figure 11(a-b) as quantitative comparisons show that there still is a significant gap between DVC-FE and DVC results. This gap increases slowly by reaching the ultimate loading steps. Similarly, the displacement difference is significantly larger than the displacement resolution (see Figure 7). Locally, the differences are mainly concentrated around debond areas (*i.e.,* matrix-nodule interfaces). It is hence important to consider more carefully the nodules and their impact both on the load carrying capacity of the material, and void growth. Additionally, the increase of the error at late loading steps indicates the inability of the microscale constitutive models used for the matrix material to capture the accel-

eration of void growth, and the subsequent void coalescence. This observation calls for more advanced plasticity models at the microscale that can capture the complex multiscale plastic flow localization in the matrix. The growth of a minor void population and damage at a lower scale could also be a possible explanation. Thus, additional material parameters should be introduced for the matrix material, and the present procedure should be extended to allow for the identification of these material parameters.

These developments will extensively rely on the DVC-FE method and its ability to provide experimentally measured boundary conditions for micromechanical simulations, and then compute local and relevant error estimators to assess the validity of these simulations. The extension of the Integrated-DIC framework to 4D analyses [57] will also be considered to conduct inverse analyses based on these error measurements and identify material parameters at the microscale.

4.2. Comparisons with wFE and sFE results

For quantitative comparisons between the DVC-FE method and its two alternatives used in this paper, two approaches are proposed. In the first approach, as commonly carried out by most authors, void growth curves are compared, giving only average quantities and global error indicators [65, 17, 18, 6, 66, 8]. The second approach aims to study which method is closer to experimental observations based on local differences. These local errors are computed by reducing the kinematic data for each simulation back to gray level residuals. This requires to extend the procedure already applied to DVC and DVC-FE kinematic data to the wFE and sFE methods.

4.2.1. Global error indicators

Void growth is defined by the following relationships

$$f = \frac{\text{void volume}}{\text{ROI volume}} \quad , \quad \text{void growth} = \frac{f}{f_0} \tag{8}$$

where f_0 denotes the initial void volume fraction. Void growth curves are shown in Figure 13. The EXP curve is obtained by computing void growth in processed

laminography images (*i.e.,* images with smooth signed distance functions as in Figure 4(b)). The 3D box where this experimental void growth is computed remains fixed to the initial ROI. The wFE and sFE curves correspond to simulations using material properties based only on load data (first line of Table 2), while the wFE I-DIC and sFE I-DIC curves correspond to simulations using material properties based on Integrated-DIC calibration (second line of Table 2).

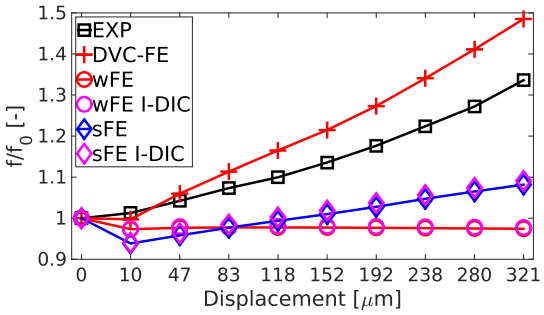

Figure 13: Void volume change curves for all the approaches investigated in this paper

Many of the numerical results show an important decrease of the porosity f at the first loading step, which is not observed for the experimental curve. This is due to the fact that remeshing is extensively used for all simulations. This remeshing has the consequence that interfaces can be slightly smoothened, and void volume can be diffused. Apart from this numerical issue, the curves reveal significant void growth with increasing load for DVC-FE and sFE results, while nearly no void growth occurs in the wFE simulation. This effect can be explained by the fact that the computation used to obtain displacement boundary conditions for the wFE simulation does not take into account damage and the subsequent volume change in the ROI. Hence, the displacement fields that are transferred to the ROI in this case are incompressible in the plastic regime, and neither the void volume nor the ROI volume can evolve. This effect calls for more advanced models (*i.e.,* including damage) to be used at the macroscopic scale.

Regarding comparisons with the experimental curve, void growth seems to be overestimated with the DVC-FE method. This can be explained by the fact that nodules are considered as voids in the simulations, while in reality only the voids nucleated after debonding of nodule/matrix interfaces grow (see Figure 9). Thus, it can be assumed that all curves would have a slightly lower slope if nodules were taken into account. The DVC-FE method is the only one that shows a void growth similar to that observed in the experiment.

The comparison between DVC-FE and sFE results using the proposed procedure shows that although void growth and the compressibility effects induced by the presence of voids are taken into account in the sFE method, this void growth is not as significant as with the DVC-FE method. In particular, the slopes of the wFE and sFE curves are clearly lower than what is observed experimentally. Both results are not improved when using Integrated-DIC material parameters. The influence of material parameters seems to be negligible in the present case. This observation remains to be confirmed with local error measurements.

4.2.2. Local error indicators

In order to compare wFE and sFE kinematic fields with X-ray images, special care is taken to subtract the rigid body motions from wFE/sFE calculated displacement fields followed by applying the corresponding rigid body motions measured by DVC. First, mean deformation gradients over the ROI for DVC and FE displacement fields are calculated. By employing a polar decomposition on the latter, FE and DVC rotations are evaluated while the mean values of kinematic fields represent the corresponding translations. From the initial FE displacement solutions then are subtracted mean FE translations and rotations and added the corresponding mean DVC translations and rotations. Hence, from the wFE/sFE displacements fields, rigid body motions originating from the FE simulations are first eliminated, and then rigid body motions associated with the experiment (*i.e.,* measured with DVC) are applied. This is performed in order to have equal conditions for all presented methods when reducing them to gray level residual images. The resulting errors are shown in Figures 14

and 11(c-d) while the displacement difference between DVC measurements and wFE calculated fields is shown in Figure 12(b).

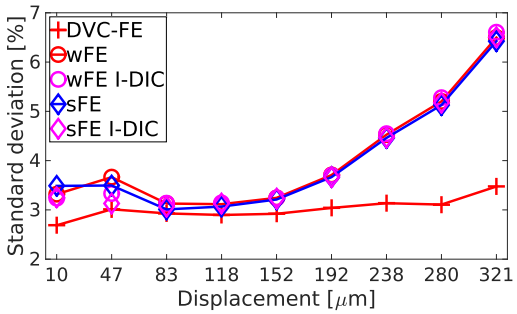

Figure 14: Standard deviation for the dimensionless gray level residual fields for all loading steps and investigated cases

Surprisingly, although sFE yields slightly better results than wFE, independently of the material parameters, this difference is negligible. This means that although the sFE method predicts a void growth that is globally closer to experimental data, the shape of these voids is inexact. Therefore, errors that do not appear in global measurements are revealed by local measurements, thereby underlining the interest of the present methodology. The small difference between wFE and sFE results could mean that the constitutive model used at the macroscale corresponds well to the homogenized mechanical response obtained in the ROI, where microscale constitutive models are used.

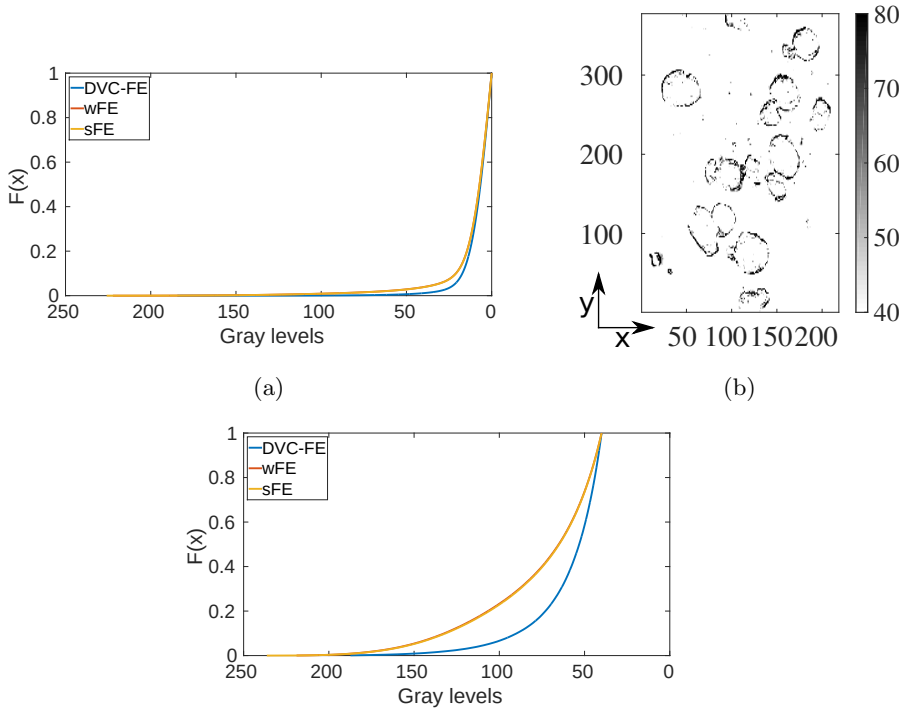

Figure 15: Cumulative distribution of gray level residuals at the last incremental loading step considering to (a) all supervoxels, (c) only supervoxels with gray level residuals higher than 40. In (b), the absolute gray level differences for the sFE method with residuals higher than 40 are shown for the same Z midsection as Figure 11(d)

Regarding the comparison between sFE/wFE and DVC-FE, the gap is increasing during the load history, ending with a deviation that is twice higher with the sFE/wFE methods than with DVC-FE. This confirms the tendency that was observed based on void growth curves. To have a more precise idea of this gap, the cumulative gray level residuals distribution is shown in Figure 15(a) for the last loading step. This difference does not seem important because it takes into account a large number of supervoxels belonging to the matrix, where contrast is low. This observation is illustrated in Figure 15(b), where only gray level residuals higher than 40 are shown, hence discarding most supervoxels of the matrix. The cumulative distribution taking into account only the remaining

supervoxels (*i.e.,* close to voids or nodules) is shown in Figure 15(c). It reveals an important difference between the DVC-FE results and those obtained with the sFE/wFE methods. The residual is doubled with the latter. This underlines the inability of macro simulations to precisely describe all the micro localization phenomena occurring in the ROI both between the machined holes and the nodules, and between the nodules themselves with the chosen constitutive models. There are nearly zero differences in the center of the ROI in Figure 12(b), which indicates that the position of the macroshear band (*i.e.,* between the machined holes) is properly captured by wFE simulations, as well as the kinematics within that band. In the same figure, more significant differences are observed in the rest of the ROI compared with DVC-FE simulations.

Overall, the use of Integrated-DIC material parameters for wFE and sFE methods slightly improves the results. As expected in Section 2.3.2, this gain is concentrated at lower strains while at higher strains the influence of these material parameters is negligible. Paint cracking and subsequent DIC convergence issues from 2D images (test (A)) could be responsible for decreasing Integrated-DIC performance at late loading steps. This observation adds to the interest for the DVC method, which relies directly on the contrast of the material. Thus, the way the material parameters are identified herein improves the results but only slightly.

Using more complex macroscale constitutive models would certainly improve the results obtained using the wFE and sFE methods. This would also increase the need for identification methods such as Integrated-DIC that take into account field measurements. For instance, the inability of both wFE and sFE methods to correctly predict plastic localization could be linked to an anisotropy of the yield surface at the macroscale, due to the presence of the nodules. Damage and the subsequent volume changes of the homogenized material should also be considered, due to debonding of the nodules from the matrix. These remarks stress out the importance of understanding the influence of the microstructure on the mechanical response of the homogenized material. Therefore, a numerical validation procedure for micromechanical simulations that does not rely on

any macroscopic constitutive model, such as the DVC-FE method, is of great interest.

5. Conclusion

The present paper discusses different choices of boundary conditions for micromechanical Finite Element (FE) simulations based on 3D X-ray data. Because it would require meshes of more than 100 million elements, Direct Numerical Simulation (DNS) is discarded and methods allowing the microstructure to be meshed only in a small Region of Interest (ROI), instead of the whole specimen, are considered. The accuracy of these methods is analyzed based on global and local error estimators relative to the 3D X-ray data acquired at consecutive loading steps for the same microstructure. The latter corresponds to *new* experimental results on a nodular cast iron specimen with two machined holes. Due to the 45° alignment of the machined holes with respect to the tensile direction, a macroscopic shear band develops between the holes. Within that macroscopic shear band, ductile fracture due to the nucleation (*i.e.,* by debonding of the nodules), growth and coalescence of microscopic voids is observed.

- In an earlier work [28], it was proposed to measure boundary conditions for micromechanical simulations via Digital Volume Correlation (DVC) directly from consecutive 3D X-ray images. Promising results were obtained for a tensile experiment on a specimen with a central hole. The results presented herein show that this DVC-FE method remains very accurate with a shear band going traversing the ROI (Figure 8). Global gray level residuals indicate an increase of the error at late loading steps, which is due to void coalescence (Figure 13). Local residuals show that these errors are located close to the debond areas around the nodules, hence calling for more relevant micromechanical models.

- A second method, which is referred to as weak FE (wFE), consists of first conducting an FE simulation at the specimen scale, considering a

totally homogeneous material, and then using the displacement fields from this first simulation to drive a second simulation at the ROI scale. It is proposed to identify material parameters for the specimen scale simulation based only on load data, and then on both load data and 2D surface images. Independently of the identification method, results show that the wFE method leads to a significant underestimation of void growth, as there is no global void volume change in wFE results (Figure 13). The slight improvement of the results when using a material parameter identification method that also takes into account 2D surface images indicates that the investigation of more relevant constitutive models for the specimen scale simulation is worth considering.

- Another method, which is coined strong FE (sFE), consists of embedding the ROI mesh in the specimen mesh. Macroscale constitutive models are used for the out-of-ROI material where the microstructure is not meshed, while microscale constitutive models are used inside the ROI where it is meshed. Void volume change curves indicate a significantly increased void growth compared to wFE results. However, local residuals indicate no significant improvement. This proves that while voids in the sFE simulation grow at a rate that is closer to the experimental observations than in wFE results, the shape of these voids is not accurately predicted. Once again, a slight improvement of the results is observed in the first loading steps when using a material parameters identification method that also takes into account 2D surface images.

As a conclusion, the dependence of both sFE and wFE methods on a specimen scale simulation and a corresponding macroscale constitutive model constitute their main limitation. Although the macroscale constitutive model used herein could be improved, such task is not obvious, especially as large plastic strains and complex damage phenomena are observed locally. This limitation of both sFE and wFE methods is also the main advantage of the DVC-FE method since DVC measurements avoid the use of a specimen scale simulation and a

corresponding macroscale constitutive model.

It is worth mentioning that since the DVC-FE method requires *in-situ* 3D X-ray imaging, it is hardly applicable to thick specimens and industrial applications. Future work will hence lean toward the use of this DVC-FE method for small specimens in order to study more relevant micromechanical models and identify material parameters for these models. These enhanced micromechanical models could then be the basis for the investigation of more relevant constitutive models to be used at the macroscale in, say, wFE and sFE methods. Such approach is likely to be applicable to other materials where micromechanical modeling is gaining an increasing interest, such as metallic foams and composite materials for instance.

6. Acknowledgments

This work was performed within the COMINSIDE project funded by the French Agence Nationale de la Recherche (ANR-14-CE07-0034-02 grant). The authors also acknowledge the European Synchrotron Radiation Facility for provision of beamtime at beamline ID15, experiment ME 1366. It is also a pleasure to acknowledge the support of BPI France ("DICCIT" project), and of the Carnot M.I.N.E.S institute ("CORTEX" project). M. Kuna and L. Zybell from IMFD, TU Freiberg are thanked for materials supply and machining as well as for scientific discussions.

References

[1] S. Avril, M. Bonnet, A.-S. Bretelle, M. Grédiac, F. Hild, P. Ienny, F. Latourte, D. Lemosse, S. Pagano, E. Pagnacco, F. Pierron, Overview of Identification Methods of Mechanical Parameters Based on Full-field Measurements, Experimental Mechanics 48 (4) (2008) 381–402.

[2] C. Tekoğlu, J. W. Hutchinson, T. Pardoen, On localization and void coalescence as a precursor to ductile fracture., Philosophical transactions. Series A, Mathematical, physical, and engineering sciences 373 (2038).

[3] A. Pineau, A. Benzerga, T. Pardoen, Failure of metals I: Brittle and ductile fracture, Acta Materialia 107 (January) (2016) 424–483.

[4] P.-O. Bouchard, L. Bourgeon, H. Lachapèle, E. Maire, C. Verdu, R. Forestier, R. Logé, On the influence of particle distribution and reverse loading on damage mechanisms of ductile steels, Materials Science and Engineering: A 496 (1-2) (2008) 223–233.

[5] A. Weck, D. Wilkinson, Experimental investigation of void coalescence in metallic sheets containing laser drilled holes, Acta Materialia 56 (8) (2008) 1774–1784.

[6] T.-S. Cao, E. Maire, C. Verdu, C. Bobadilla, P. Lasne, P. Montmitonnet, P.-O. Bouchard, Characterization of ductile damage for a high carbon steel using 3D X-ray micro-tomography and mechanical tests – Application to the identification of a shear modified GTN model, Computational Materials Science 84 (2014) 175–187.

[7] L. Lecarme, E. Maire, A. Kumar K.C., C. De Vleeschouwer, L. Jacques, A. Simar, T. Pardoen, Heterogenous void growth revealed by in situ 3-D X-ray microtomography using automatic cavity tracking, Acta Materialia 63 (2014) 130–139.

[8] D. Seo, H. Toda, M. Kobayashi, K. Uesugi, A. Takeuchi, Y. Suzuki, In Situ Observation of Void Nucleation and Growth in a Steel using X-ray Tomography, ISIJ International 55 (7) (2015) 1474–1482.

[9] F. Hannard, T. Pardoen, E. Maire, C. Le Bourlot, R. Mokso, A. Simar, Characterization and micromechanical modelling of microstructural heterogeneity effects on ductile fracture of 6xxx aluminium alloys, Acta Materialia 103 (2016) 558–572.

[10] A. L. Gurson, Plastic Flow and Fracture Behavior of Ductile Materials Incorporating Void Nucleation, Growth, and Interaction, Ph.D. thesis, Brown University (1975).

[11] M. Gologanu, J.-B. Leblond, J. Devaux, Approximate models for ductile metals containing non-spherical voids. Case of axisymmetric prolate ellipsoidal cavities, Journal of the Mechanics and Physics of Solids 41 (11) (1993) 1723–1754.

[12] A. A. Benzerga, J. B. Leblond, Ductile Fracture by Void Growth to Coalescence, Advances in Applied Mechanics 44 (2010) 169–305.

[13] F. Scheyvaerts, P. Onck, C. Tekoglu, T. Pardoen, The growth and coalescence of ellipsoidal voids in plane strain under combined shear and tension, Journal of the Mechanics and Physics of Solids 59 (2) (2011) 373–397.

[14] A. Needleman, V. Tvergaard, An analysis of ductile rupture in notched bars, Journal of the Mechanics and Physics of Solids 32 (6) (1984) 461–490.

[15] E. Bosco, V. G. Kouznetsova, M. G. D. Geers, Multi-scale computational homogenization-localization for propagating discontinuities using X-FEM, International Journal for Numerical Methods in Engineering 102 (3-4) (2015) 496–527.

[16] T.-S. Cao, M. Mazière, K. Danas, J. Besson, A model for ductile damage prediction at low stress triaxialities incorporating void shape change and void rotation, International Journal of Solids and Structures 63 (2015) 240–263.

[17] C. Landron, O. Bouaziz, E. Maire, J. Adrien, Characterization and modeling of void nucleation by interface decohesion in dual phase steels, Scripta Materialia 63 (10) (2010) 973–976.

[18] J. Fansi, T. Balan, X. Lemoine, E. Maire, C. Landron, O. Bouaziz, M. Ben Bettaieb, A. Marie Habraken, Numerical investigation and experimental validation of physically based advanced GTN model for DP steels, Materials Science and Engineering: A 569 (2013) 1–12.

[19] R. Tian, S. Chan, S. Tang, A. M. Kopacz, J. S. Wang, H. J. Jou, L. Siad, L. E. Lindgren, G. B. Olson, W. K. Liu, A multiresolution continuum simulation of the ductile fracture process, Journal of the Mechanics and Physics of Solids 58 (10) (2010) 1681–1700.

[20] A. Hosokawa, D. S. Wilkinson, J. Kang, M. Kobayashi, H. Toda, Void growth and coalescence in model materials investigated by high-resolution X-ray microtomography, International Journal of Fracture 181 (1) (2013) 51–66.

[21] S. Tang, A. M. Kopacz, S. Chan O'Keeffe, G. B. Olson, W. K. Liu, Three-dimensional ductile fracture analysis with a hybrid multiresolution approach and microtomography, Journal of the Mechanics and Physics of Solids 61 (11) (2013) 2108–2124.

[22] Y. Alinaghian, M. Asadi, A. Weck, Effect of pre-strain and work hardening rate on void growth and coalescence in AA5052, International Journal of Plasticity 53 (2014) 193–205.

[23] G. Hütter, L. Zybell, M. Kuna, Size effects due to secondary voids during ductile crack propagation, International Journal of Solids and Structures 51 (3-4) (2014) 839–847.

[24] S. C. O'Keeffe, S. Tang, A. M. Kopacz, J. Smith, D. J. Rowenhorst, G. Spanos, W. K. Liu, G. B. Olson, Multiscale ductile fracture integrating tomographic characterization and 3-D simulation, Acta Materialia 82 (2015) 503–510.

[25] V. Tvergaard, J. W. Hutchinson, Two mechanisms of ductile fracture: Void by void growth versus multiple void interaction, International Journal of Solids and Structures 39 (13-14) (2002) 3581–3597.

[26] J. Bandstra, D. Koss, A. Geltmacher, P. Matic, R. Everett, Modeling void coalescence during ductile fracture of a steel, Materials Science and Engineering: A 366 (2) (2004) 269–281.

[27] M. Kaye, C. Puncreobutr, P. D. Lee, D. S. Balint, T. Connolley, D. Farrugia, J. Lin, A new parameter for modelling three-dimensional damage evolution validated by synchrotron tomography, Acta Materialia 61 (20) (2013) 7616–7623.

[28] A. Buljac, M. Shakoor, J. Neggers, L. Helfen, M. Bernacki, P.-O. Bouchard, T. F. Morgeneyer, F. Hild, Numerical Validation Framework for Micromechanical Simulations based on Synchrotron 3D Imaging, Computational Mechanics (in press). doi:10.1007/s00466-016-1357-0.

[29] S. Roux, F. Hild, P. Viot, D. Bernard, Three-dimensional image correlation from X-ray computed tomography of solid foam, Composites Part A: Applied Science and Manufacturing 39 (8) (2008) 1253–1265.

[30] J. Rannou, N. Limodin, J. Réthoré, A. Gravouil, W. Ludwig, M.-C. Baïetto-Dubourg, J.-Y. Buffière, A. Combescure, F. Hild, S. Roux, Three dimensional experimental and numerical multiscale analysis of a fatigue crack, Computer Methods in Applied Mechanics and Engineering 199 (21-22) (2010) 1307–1325.

[31] A. Buljac, T. Taillandier-Thomas, T. F. Morgeneyer, L. Helfen, S. Roux, F. Hild, Slant strained band development during flat to slant crack transition in AA 2198 T8 sheet: in situ 3D measurements, International Journal of Fracture 200 (1) (2016) 49–62.

[32] F. Mathieu, H. Leclerc, F. Hild, S. Roux, Estimation of Elastoplastic Parameters via Weighted FEMU and Integrated-DIC, Experimental Mechanics 55 (1) (2015) 105–119.

[33] M. J. Dong, C. Prioul, D. François, Damage effect on the fracture toughness of nodular cast iron: Part I. Damage characterization and plastic flow stress modeling, Metallurgical and Materials Transactions A 28 (11) (1997) 2245–2254.

[34] G. Hütter, L. Zybell, M. Kuna, Micromechanisms of fracture in nodular cast iron: From experimental findings towards modeling strategies – A review, Engineering Fracture Mechanics 144 (2015) 118–141.

[35] Z. Tomičević, J. Kodvanj, F. Hild, Characterization of the nonlinear behavior of nodular graphite cast iron via inverse identification–Analysis of uniaxial tests, European Journal of Mechanics - A/Solids 59 (2016) 140–154.

[36] K. Zhang, J. Bai, D. François, Ductile fracture of materials with high void volume fraction, International Journal of Solids and Structures 36 (23) (1999) 3407–3425.

[37] N. Bonora, A. Ruggiero, Micromechanical modeling of ductile cast iron incorporating damage. Part I: Ferritic ductile cast iron, International Journal of Solids and Structures 42 (5-6) (2005) 1401–1424.

[38] A. Myagotin, A. Voropaev, L. Helfen, D. Hänschke, T. Baumbach, Efficient Volume Reconstruction for Parallel-Beam Computed Laminography by Filtered Backprojection on Multi-Core Clusters, IEEE Trans. Image Process. 22 (12) (2013) 5348–5361.

[39] M. Vogelgesang, T. Farago, T. F. Morgeneyer, L. Helfen, T. dos Santos Rolo, A. Myagotin, T. Baumbach, Real-time image content based beamline control for smart 4D X-ray imaging, Journal of Synchrotron Radiation 23 (2016) 1254–1263.

[40] C. Tasan, J. Hoefnagels, M. Geers, Identification of the continuum damage parameter: An experimental challenge in modeling damage evolution, Acta Materialia 60 (8) (2012) 3581–3589.

[41] E. Roux, M. Bernacki, P.-O. Bouchard, A level-set and anisotropic adaptive remeshing strategy for the modeling of void growth under large plastic strain, Computational Materials Science 68 (2013) 32–46.

[42] E. Roux, M. Shakoor, M. Bernacki, P.-O. Bouchard, A new finite element approach for modelling ductile damage void nucleation and growth—analysis of loading path effect on damage mechanisms, Modelling and Simulation in Materials Science and Engineering 22 (7) (2014) 075001.

[43] M. Shakoor, B. Scholtes, P.-O. Bouchard, M. Bernacki, An efficient and parallel level set reinitialization method: Application to micromechanics and microstructural evolutions, Applied Mathematical Modelling 39 (23-24) (2015) 7291–7302.

[44] M. Shakoor, M. Bernacki, P.-O. Bouchard, A new body-fitted immersed volume method for the modeling of ductile fracture at the microscale: Analysis of void clusters and stress state effects on coalescence, Engineering Fracture Mechanics 147 (2015) 398–417.

[45] M. Shakoor, P.-O. Bouchard, M. Bernacki, An adaptive Level-Set Method with enhanced volume conservation for simulations in multiphase domains, International Journal for Numerical Methods in Engineering (in press). doi:10.1002/nme.5297.

[46] J. Schindelin, I. Arganda-Carreras, E. Frise, V. Kaynig, M. Longair, T. Pietzsch, S. Preibisch, C. Rueden, S. Saalfeld, B. Schmid, J.-Y. Tinevez, D. J. White, V. Hartenstein, K. Eliceiri, P. Tomancak, A. Cardona, Fiji: an open-source platform for biological-image analysis, Nature Methods 9 (7) (2012) 676–682.

[47] C. A. Schneider, W. S. Rasband, K. W. Eliceiri, NIH Image to ImageJ: 25 years of image analysis, Nature Methods 9 (7) (2012) 671–675.

[48] D. Boffi, F. Brezzi, L. F. Demkowicz, R. G. Durán, R. S. Falk, M. Fortin, Mixed Finite Elements, Compatibility Conditions, and Applications, Vol. 1939 of Lecture Notes in Mathematics, Springer Berlin Heidelberg, Berlin, Heidelberg, 2008.

[49] R. H. Wagoner, J. L. Chenot, Metal Forming Analysis, Cambridge University Press, 2001.

[50] R. Storn, K. Price, Differential Evolution - A Simple and Efficient Heuristic for Global Optimization over Continuous Spaces, Journal of Global Optimization 11 (4) (1997) 341–359.

[51] M. Grédiac, F. Hild (Eds.), Full-Field Measurements and Identification in Solid Mechanics, John Wiley & Sons, Inc., Hoboken, NJ USA, 2013.

[52] E. Roux, P.-O. Bouchard, On the interest of using full field measurements in ductile damage model calibration, International Journal of Solids and Structures 72 (2015) 50–62.

[53] G. Besnard, F. Hild, S. Roux, "Finite-element" displacement fields analysis from digital images: Application to Portevin-Le Chatelier bands, Experimental Mechanics 46 (2006) 789–803.

[54] F. Hild, S. Roux, Comparison of local and global approaches to digital image correlation, Experimental Mechanics 52 (9) (2012) 1503–1519.

[55] M. Kahziz, T. Morgeneyer, M. Maziere, L. Helfen, O. Bouaziz, E. Maire, In situ 3D synchrotron laminography assessment of edge fracture in DP steels: quantitative and numerical analysis, Experimental Mechanics 56 (2016) 177–195.

[56] J. Neggers, J. P. M. Hoefnagels, M. G. D. Geers, F. Hild, S. Roux, Time-resolved integrated digital image correlation, International Journal for Numerical Methods in Engineering 103 (3) (2015) 157–182.

[57] F. Hild, A. Bouterf, L. Chamoin, F. Mathieu, J. Neggers, F. Pled, Z. Tomičević, S. Roux, Toward 4D mechanical correlation, Advanced Modeling and Simulation in Engineering Sciences 3 (1) (2016) 17.

[58] A. Tarantola, Inverse Problem Theory: Methods for Data Fitting and Model Parameter Estimation, Elseiver Applied Science, 1987.

[59] H. Leclerc, J. Neggers, F. Mathieu, S. Roux, F. Hild, Correli 3.0, IDDN.FR.001.520008.000.S.P.2015.000.31500, Agence pour la Protection des Programmes, Paris (France) (2015).

[60] A. Hosokawa, D. S. Wilkinson, J. Kang, E. Maire, Onset of void coalescence in uniaxial tension studied by continuous X-ray tomography, Acta Materialia 61 (4) (2013) 1021–1036.

[61] F. Xu, L. Helfen, T. Baumbach, H. Suhonen, Comparison of image quality in computed laminography and tomography, Optics Express 20 (2012) 794–806.

[62] S. Roux, F. Hild, P. Viot, D. Bernard, Three dimensional image correlation from X-Ray computed tomography of solid foam, Composites Part A: Applied Science and Manufacturing 39 (8) (2008) 1253–1265.

[63] T. Morgeneyer, L. Helfen, H. Mubarak, F. Hild, 3D Digital Volume Correlation of Synchrotron Radiation Laminography images of ductile crack initiation: An initial feasibility study, Experimental Mechanics 53 (4) (2013) 543–556.

[64] H. Leclerc, J. Périé, F. Hild, S. Roux, Digital volume correlation: What are the limits to the spatial resolution?, Mechanics & Industry 13 (2012) 361–371.

[65] L. Babout, Y. Bréchet, E. Maire, R. Fougères, On the competition between particle fracture and particle decohesion in metal matrix composites, Acta Materialia 52 (15) (2004) 4517–4525.

[66] D. Seo, H. Toda, M. Kobayashi, K. Uesugi, A. Takeuchi, Y. Suzuki, Three-Dimensional Investigation of Void Coalescence in Free-Cutting Steel using X-ray Tomography, ISIJ International 55 (7) (2015) 1483–1488.